Bayesian tracking of elongated structures in 3D images

Michiel Schaap, Ihor Smal, Coert Metz, Theo van Walsum, and Wiro Niessen

Biomedical Imaging Group Rotterdam,
Departments of Radiology and Medical Informatics
Erasmus MC - University Medical Center Rotterdam
{michiel.schaap,i.smal,c.metz,t.vanwalsum,w.niessen}@erasmusmc.nl

Abstract. Tracking of tubular elongated structures is an important goal in a wide range of biomedical imaging applications. A Bayesian tube tracking algorithm is presented that allows to easily incorporate a priori knowledge. Because probabilistic tube tracking algorithms are computationally complex, steps towards a computational efficient implementation are suggested in this paper.
The algorithm is evaluated on 2D and 3D synthetic data with different noise levels and clinical CTA data. The approach shows good performance on data with high levels of Gaussian noise.

Key words: Bayesian tracking, efficient, high noise, CTA.

1 Introduction

Tracking of tubular elongated structures is an important goal in a wide range of biomedical imaging applications. For example, vessel tracking in medical images has received considerably attention, as it can be used as a preprocessing step towards stenosis evaluation and grading, by generating multi-planar reformatted images [1]. For a review of several vessel tracking methodologies, we refer to papers of Kirbas and Quek [2], Suri et al. [3], and Florin et al. [4].

State-of-the-art methods to track elongated structures use a priori knowledge of the tubular appearance in the image and the geometry of the tube. Appearance information include zeroth, first and second order image intensity information (e.g. in [5]) and geometric measures include the minimal surface curvature of the tracked tube (see, for example, [6]).

Until recently only deterministic approaches were presented, which take only one assumption of the track configuration into account during tracking. The path is found by updating the track to the most probable configuration at each iteration of the method. This may lead to situations where imaging data that locally does not meet the a priori assumptions, e.g. owing to pathologies, corrupted or missing data, can steer the track to incorrect configurations.

By taking into account multiple hypotheses during tracking this problem can be circumvented. Probabilistic approaches to track elongated structures using

Monte Carlo sampling (particle filtering)[4, 7] have been presented in order to search globally for the path that reflects the priors as good as possible. It has been reported that these methods can better overcome corrupted and missing data than deterministic approaches. Because the probabilistic methods track multiple hypotheses at once, they are computationally more complex than deterministic approaches.

The novelty of the current paper is twofold. First, it presents a Bayesian tracking approach which allows to easily incorporate a priori knowledge. It is shown that this approach enables tracking of tubular structures, even in the case of very high noise levels. Second, to overcome the computational complexity of probabilistic tracking algorithms, a computationally efficient implementation is proposed.

2 Bayesian tracking of elongated structures

In this section the iterative Bayesian tracking approach is presented. We will first discuss the tubular model that we employ. Subsequently we will describe the observation model, hypotheses prediction and update step.

2.1 Tube model

Out tracking method will consider a tube as a series of tube segments. A tube segment at iteration t is described by its location $\boldsymbol{p}_t = (x_t, y_t, z_t)^T$, orientation $\boldsymbol{v}_t = (\theta_t, \phi_t)$, radius r_t, and average intensity I_t. Thus each tube segment is characterized by a state vector $\mathbf{x}_t = (\boldsymbol{p}_t, \boldsymbol{v}_t, r_t, I_t)^T$. This results in a tube configuration described by $\mathbf{x}_{0:t} \triangleq \{\mathbf{x}_0, \ldots, \mathbf{x}_t\}$, see Figure 1(a).

With every tube segment we associate a region of interest, defined by the components $\boldsymbol{p}_t$, r_t, and $\boldsymbol{v}_t$ of $\mathbf{x}_t$ (see Fig. 1b). Subsequently, we let $\mathbf{z}_t$ denote the image measurements within this ROI. Hence, all measurements corresponding to tube $\mathbf{x}_{0:t}$ are denoted with $\mathbf{z}_{0:t}$. As an example, the image intensity within the tube and outside the tube (I_{in} and I_{out}) are computed, using nearest neighbor interpolation, from $\mathbf{z}_t$, see Figure 1(b).

2.2 Observation model

In our observation model, we assume tubes to be bright relative to their background. Given the tube segment $\mathbf{x}_t$ and the measurements $\mathbf{z}_t$, the likelihood of the measurements given the state $\mathbf{x}_t$, $p(\mathbf{z}_t|\mathbf{x}_t)$, is constructed as follows:

$$p(\mathbf{z}_t|\mathbf{x}_t) \propto p(\mathbf{z}_t|\boldsymbol{p}_t, \boldsymbol{v}_t, r_t, I_t) = p(I_{\text{in}}, I_{\text{out}})\mathcal{N}(I_{\text{in}}|I_t, \sigma_\varsigma^2), \tag{1}$$

where

$$p(I_{\text{in}}, I_{\text{out}}) = \begin{cases} (\frac{I_{\text{in}} - I_{\text{out}}}{I_c})^s, & I_{\text{in}} > I_{\text{out}}, \\ 0, & I_{\text{in}} \leq I_{\text{out}}. \end{cases} \tag{2}$$

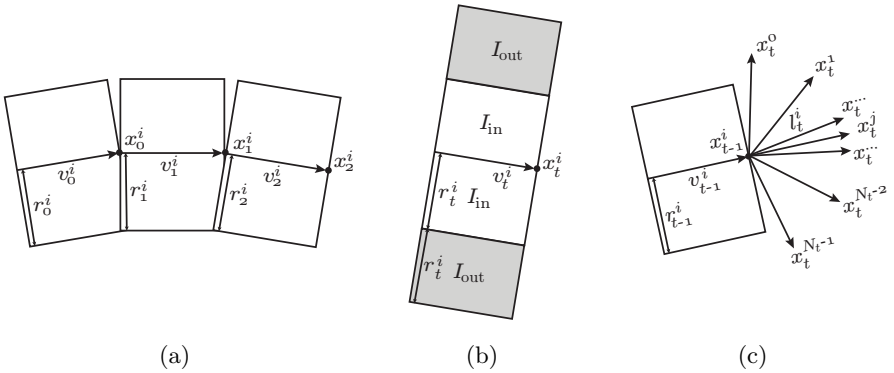

Fig. 1. Figure (a) shows a part of the tube configuration $\mathbf{x}_{0:t}$. Figure (b) demonstrates how the values I_{in} and I_{out} are obtained from patch $\mathbf{z}_t$. The prediction of new tubular segments, as explained in Section 2.3, is presented in Figure (c).

with I_c and s contrast regulating parameters and $\mathcal{N}(.|\mu, \sigma^2)$ a real normal distribution with mean μ and variance σ^2. The term $\mathcal{N}(I_{\text{in}}|I_t, \sigma_\varsigma^2)$ describes the likelihood that the measured intensity I_{in} resembles the intensity I_t, which is predicted from the previous iterations using the Kalman filter described in Section 2.4.

2.3 Prediction

Using the Bayesian rule, the probability density function (pdf) $p(\mathbf{x}_{0:t}|\mathbf{z}_{0:t})$, that describes the posterior probability of the tube configuration, having all the observations up to iteration t can be estimated with the following recursion [8]

$$p(\mathbf{x}_{0:t}|\mathbf{z}_{0:t}) \propto p(\mathbf{x}_t|\mathbf{x}_{t-1})p(\mathbf{z}_t|\mathbf{x}_t)p(\mathbf{x}_{0:t-1}|\mathbf{z}_{0:t-1}), \tag{3}$$

where the transition prior $p(\mathbf{x}_t|\mathbf{x}_{t-1})$ is assumed to be Markovian ($\mathbf{x}_t$ only depends on $\mathbf{x}_{t-1}$ and not on any other past states) and is factorized as

$$p(\mathbf{x}_t|\mathbf{x}_{t-1}) = p(\boldsymbol{p}_t, \boldsymbol{v}_t|\boldsymbol{p}_{t-1}, \boldsymbol{v}_{t-1})p(r_t|r_{t-1})p(I_t|I_{t-1}), \tag{4}$$

The likelihood $p(\mathbf{z}_t|\mathbf{x}_t)$ relates the conditionally independent measurements at iteration t to the state $\mathbf{x}_t$, as defined in equation (1).

At each iteration step, we represent the probability of the tube configuration with a set of N_t weighted states $\boldsymbol{X}_{0:t} = \{\mathbf{x}_{0:t}^i, w_t^i\}_{i=1}^{N_t}$, thus

$$p(\mathbf{x}_{0:t}|\mathbf{z}_{0:t}) = \sum_{i=1}^{N_t} w_t^i \delta(\mathbf{x}_{0:t} - \mathbf{x}_{0:t}^i), \tag{5}$$

where $\delta(\cdot)$ is the Dirac delta function and the weights are normalized such that $\sum_{i=1}^{N_t} w_t^i = 1$.

In each iteration we use the variance of the weights w_t^i to determine how many and which hypotheses should be kept in the next iteration. The N_e most probable hypotheses are kept according to the weights $w_t^i, i \in \{1, ..., N_t\}$, where

$$N_e = \frac{1}{\sum_i^{N_t} (w_t^i)^2} \tag{6}$$

From each of these states, $N_t^i = \text{nint}(w_t^i N)$ new states are created, where nint(.) denotes a nearest integer round and N is pre-defined and describes the maximum number of hypotheses created. This approach will keep only the relevant hypotheses and effectively distribute them according to the described pdf.

2.4 Update

In the update step, prior knowledge on the curvature of the centerline, the variance of the tube radius along the centerline, the intensity variance in the tube and the contrast-to-noise ratio in the image are incorporated. This is achieved as follows.

The formation of the N_t^i new hypotheses $\mathbf{x}_t^j$, $j = \{0, ..., N_t^i - 1\}$, at iteration t from the previous hypothesis $\mathbf{x}_t^i$ consist of a transition to a new position $\boldsymbol{p}_t$, which is deterministically defined by

$$\boldsymbol{p}_t^j = \boldsymbol{p}_{t-1}^i + R_z(\theta_{t-1}) R_y(\phi_{t-1}) R_z(\vartheta_t^j) R_y(\varphi_t^j) (0, 0, l_t^i)^T \tag{7}$$

where $R_z(.)$ and $R_y(.)$ are rotation matrices around the z- and y-axis [9]. The length of a tube segment l_t^i depends on the radius of the tube r_{t-1}^i and a predefined parameter α.

$$l_t^i = \frac{r_{t-1}^i}{\tan(\alpha)} \tag{8}$$

Figure 1(c) gives a schematic explanation of the transition in eq. (7). The angles $(\vartheta_t^j, \varphi_t^j)$ describe a point in the local spherical coordinate system with the z-axis orientated in the direction of $\boldsymbol{v}_{t-1}^i$ and origin at $\boldsymbol{p}_{t-1}$. Therefore, the angle φ_t^j is equal to the enclosed angle between $\boldsymbol{v}_{t-1}$ and $\boldsymbol{v}_t$. The two angles $(\vartheta_t^j, \varphi_t^j)$ are constructed with an algorithm that uniformly distributes points on a sphere, as described by Saff and Kuijlaars [10]. This algorithm is used to distribute the N_t^i new hypotheses uniformly on the half sphere in front of $\boldsymbol{p}_{t-1}$ oriented in the direction of $\boldsymbol{v}_{t-1}$. In this case, the transition density $p(\boldsymbol{p}_t, \boldsymbol{v}_t | \boldsymbol{p}_{t-1}^i, \boldsymbol{v}_{t-1}^i)$ is given by

$$p(\boldsymbol{p}_t, \boldsymbol{v}_t | \boldsymbol{p}_{t-1}^i, \boldsymbol{v}_{t-1}^i) = \sum_{j=0}^{N_t^i - 1} \tilde{\omega_j} \delta(\boldsymbol{p}_t - \boldsymbol{p}_t^j) \tag{9}$$

where the weight $\tilde{\omega_j}$ of a given enclosed angle is given by

$$\tilde{\omega_j} = \frac{\omega(\phi_j)}{\sum_{k=0}^{N_t^i} \omega(\phi_k)} \tag{10}$$

$$\omega(\varphi) = N(\varphi|0, \sigma_\varphi^2) \tag{11}$$

with σ_φ being a pre-defined parameter.

The transition of r_t and I_t is assumed to be Markovian and described by

$$r_t = r_{t-1} + \eta_t, \tag{12}$$

$$I_t = I_{t-1} + \xi_t \tag{13}$$

where η_t and ξ_t are uncorrelated Gaussian random variables with variances σ_r^2 and σ_I^2, respectively. In this case

$$p(r_t|r_{t-1}) = \mathcal{N}(r_t|r_{t-1}, \sigma_r^2) \tag{14}$$

$$p(I_t|I_{t-1}) = \mathcal{N}(I_t|I_{t-1}, \sigma_I^2) \tag{15}$$

The observation model for the intensity I_t is a linear (conditional on the rest of the state parameters) Gaussian model given by

$$I_{\text{in}} = I_t + \varsigma_t \tag{16}$$

where $\varsigma_t \sim \mathcal{N}(\varsigma|0, \sigma_\varsigma^2)$. The model (13),(16) is a linear Gaussian model that can be solved analytically using the Kalman filter [8]

$$I_{t|t-1} = I_{t-1}, \qquad I_t = I_{t|t-1} + K_t(I_{\text{in}} - I_{t|t-1}),$$
$$P_{t|t-1} = P_{t-1} + \sigma_I^2 \qquad P_t = (1 - K_t)P_{t|t-1}$$

where P_t denotes the estimated variance of I_t and the Kalman gain $K_t = \frac{P_{t|t-1}}{P_{t|t-1}+\sigma_\varsigma^2}$.

For each prediction $I_{t|t-1}^j$ of the Kalman filter for the intensity I_{t-1}^i we estimate the radius of the tube segment r_t^j as follows

$$\hat{r}_t^j = \underset{r_t}{\operatorname{argmax}}\, p(\mathbf{z}_t|\boldsymbol{p}_t^j, \phi_t^j, r_t, I_{t|t-1})p(r_t|r_{t-1}) \tag{17}$$

Then, the Kalman update is performed for the intensity I_t with the new measurement I_{in}. If no a priori knowledge about the image intensity distribution is available, the Kalman filter is not used in the first iteration, then I_1^i is set to I_{in}.

3 Implementation details

Each of the possible new states $\mathbf{x}_t^j$ is described by a relative angle $\boldsymbol{v}_t^j$ and a radius r_t, where $r_t \in (0..R)$, with $R = r_{t-1} + \sigma_r$ being the maximum evaluated tube radius.

For each voxel in a patch around $\boldsymbol{p}_{t-1}^i$ we can easily calculate to which angle and radius combination it belongs. Using these measurements it is possible to quickly calculate for all the possible $N_t^i \times R$ combinations the values I_{in} and I_{out}. The advantage of this procedure is that each voxel in the image is accessed only once per state $\mathbf{x}_{t-1}^i$ and several redundant computations are avoided, which has computational benefits.

4 Evaluation

In this section, the developed probabilistic tracking algorithm is evaluated on 2D and 3D synthetic data, simulated computed tomography angiography (CTA) data and real CTA data.

4.1 Parameters

For all the evaluations we used fixed parameter settings that were empirically selected based on experiments on synthetic data not belonging to the test set. In these studies it was observed that the method was not sensitive to parameter changes. The following parameter settings were used, $N = 500$, $I_c = 1.0$, $s = 1.0$, $\sigma_\varphi^2 = 1.5$, $\sigma_r^2 = 2$, $\sigma_I^2 = 1000$, $\sigma_\varsigma^2 = 10$, and $\alpha = 0.25$

4.2 Initialization

The algorithm is initialized with a seed point and a radius estimation. The set of state vectors $\mathbf{X}_0$ contains two state vectors, with locations $\boldsymbol{p}_0^0$ and $\boldsymbol{p}_0^1$ equal to the seed point and radii r_0^0 and r_0^1 equal to the estimated radius. The orientations are initialized with $\boldsymbol{v}_0^0 = (0, 0)$ and $\boldsymbol{v}_0^1 = (\pi, 0)$.

4.3 2D synthetic data

In order to investigate the accuracy of the developed method as a function of image noise, a quantitative study on 2D synthetic data was carried out.

Rose has introduced a distinguishability measure MD = CNR$\sqrt{A}$ in [11], where CNR is the ratio of the contrast between an object and its background and the standard deviation of the noise in the image and A denotes the amount of voxels of the object.

For our experiments, four random tubes were created with radii and distinguishability values of respectively $r = \{2.5, 5.0, 7.5, 10\}$ pixels and MD = $\sqrt{2}\{0.5, 1.0, 1.5, 2.0\}$ pixels, resulting in 64 different test images.

These synthetic tubes were created by fitting 3rd order splines through five randomly selected points in a 2D grid of 512×512 pixels. Tubes were excluded if a part of the tube had a distance to other parts of the tube, not being direct neighbors, of less than 100 pixels or if the maximum curvature of the tube centerline was higher than 0.04 pixels^{-1}. See Figure 3(a) for an example tube.

The tubes were tracked automatically and manually which allows comparison between the obtained accuracy and the human capabilities of tracking tubes in noisy data. Four observers each annotated centerlines in 16 of the 64 images. The different radii and noise levels were equally distributed over the four observers.

In the automatic tracking, the radius was initialized at the average size of the synthetic tubes evaluated, being 6.25 pixels. It is believed that this simulates typical a priori knowledge of an expected tube size.

As an evaluation criterion we determine the root mean squared distance (RMSD) between the automatically or manually tracked tube and the centerline

of the golden standard. This number is divided by the radius of the tube in order to present the accuracy of tracking relative to the tube size (RMSD/r).

Only distances for paths where at least 95% of the track is found at a distance within twice the radius of the golden standard are taken into account. In this way the ability of tracking the tube and the accuracy of tracking is presented.

4.4 3D synthetic data

A 3D synthetic evaluation was carried out to evaluate the performance of the algorithm for tracking 3D tubes with varying radius and high image noise. A 3D synthetic tube with varying radius from $r = 4$ voxels to $r = 10$ voxels is created and Gaussian noise is added, resulting in a CNR value of 0.25 and thereby distinguishability measures of MD = 1.8 to MD = 4.4 voxels. The algorithm was initialized with a seed point at the beginning of the tube and radius was set to 7 voxels. The performance of the algorithm is evaluated by measuring the RMSD to the centerline of the synthetic tube.

4.5 Simulated CTA data

To simulate clinical data with high noise, a computed tomography angiography (CTA) artery segmentation was manually extracted from CTA data. The segmentation was given a contrast of 200 intensity units to its background, similar to the contrast of arteries in CTA. This segmentation was smoothed with a Gaussian kernel with standard deviation of 1 voxel, similar to the point spread function of CT. Afterward Gaussian noise was added, with a standard deviations of 240 intensity units, approximately eight times higher than the clinical noise value of 30 intensity units. The algorithm was initialized with a seedpoint at the approximate beginning of the tube and the radius was set to twice the (approximate) average radius of the simulated vessel. The RMSD difference to a manual tracked centerline is used as a performance measure.

4.6 Tracking in real CTA data

In order to demonstrate the applicability of the algorithm on real data, we have used the algorithm to track two arteries in a CTA dataset. We used a dataset where the imaged patient had a chronic total occlusion, meaning that an artery was blocked and (almost) no blood was passing the point of occlusion. Such a dataset is problematic for conventional deterministic algorithms, because of the lack of local image contrast. The algorithm was initialized by putting a seedpoint in the vessels and setting the radius to approximately twice the radius of the vessel.

5 Results

5.1 2D synthetic data

The results of the evaluation on 2D synthetic data are shown in Figure 2 and Table 1. Figure 2 shows the relation between the accuracy of the manually and

automatically tracked paths. Table 1 shows the performance of the manual and automatic trackings, for the four different distinguishability measures.

	Manual			Automatic		
$\frac{\text{MD}}{\sqrt{2}}$	#found	RMSD	RMSD/r	#found	RMSD	RMSD/r
0.5	14/16	3.12	0.40	5/16	2.85	0.39
1.0	16/16	1.37	0.25	16/16	1.72	0.31
1.5	16/16	1.11	0.21	16/16	1.60	0.30
2.0	16/16	1.05	0.19	16/16	1.52	0.28

Table 1. Evaluation results for the evaluation with 2D synthetic data. A tube is found if at least 95 percent of the length of the path was tracked at a distance to the golden standard of less than two times the radius of the tube. For tubes that were found both manually and automatically, the root mean squared difference (RMSD) and the root of the average of the squared ratio between distance and radius RMSD/r is shown.

For the automatically tracked path that had an overlap of less than 95%, the overlap was always less than 45%. Two of these tracks were also not found manually with an overlap of at least 95% (respectively 85% and 88%). An example of the input data and the automatic tracking is presented in Figure 3.

5.2 3D synthetic data

The algorithm tracked the full length of the path in the 3D synthetic tube. The RMSD to the golden standard was 2.3 voxels. Figure 4 visualizes this result.

5.3 Simulated CTA data

The automatically found track in the simulated CTA dataset was found with a RMSD of 1.7 voxels to the manually annotated reference standard. Figure 5 shows the simulated CTA dataset, found path and reference standard.

5.4 Clinical examples

The two clinical examples are shown in Figure 6. Both trackings were visually evaluated and found to be well within the boundary of the vessel.

6 Discussion

The evaluation on 2D synthetic data showed that the algorithm was capable of tracking tubes with a distinguishability measure MD of 1.4 with accuracies that were in the same order of magnitude as the tracking results of the human observers.

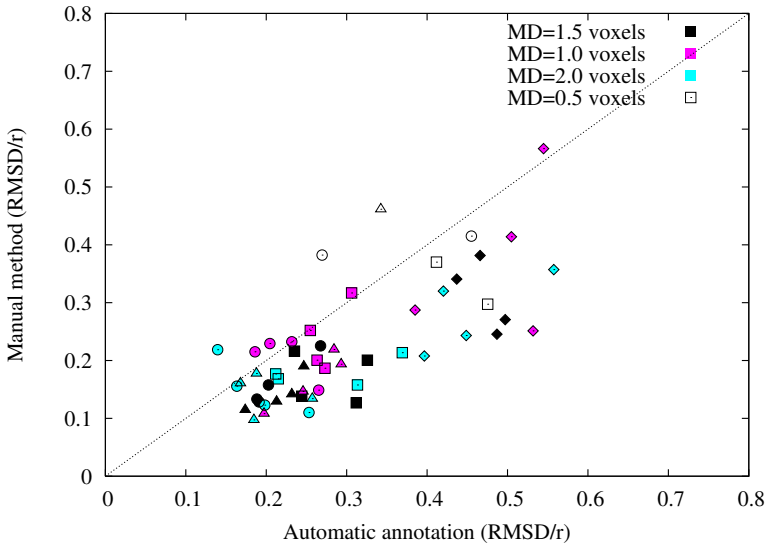

Fig. 2. Scatter plot demonstrating the relation between the accuracy, measured in RMSD/r, of the manually and automatically tracked tube centerlines. The different symbols denote different radii ($\Diamond$ = 2.5, $\square$ = 5.0, $\bigcirc$ = 7.5, $\triangle$ = 10.0, all in voxels), and different colors denote different noise levels.

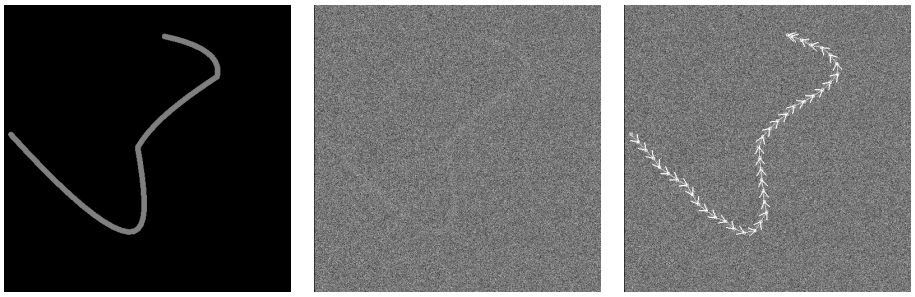

(a) (b) (c)

Fig. 3. An example of the data and results of the 2D synthetic evaluation. Figure (a) is a randomly created tube with radius of 5 voxels and 200 intensity units contrast. Figure (b) is the image after Gaussian noise with a standard deviation of 894 was added, resulting in CNR = 0.224 and $M_d = 0.5\sqrt{2}$. Figure (c) shows the tracking result of the algorithm.

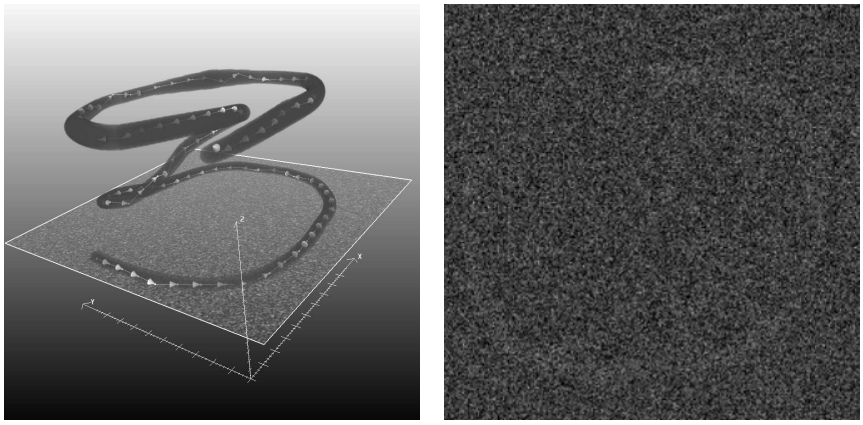

(a) (b)

Fig. 4. A demonstration of tracking with the developed algorithm of a 3D synthetic tube with radius varying between 5 and 10 voxels and CNR of 0.25. In (a) the tracking result in 3D is shown with the tube without noise and a slice of the volume with noise. (b) shows the noisy slice in 2D.

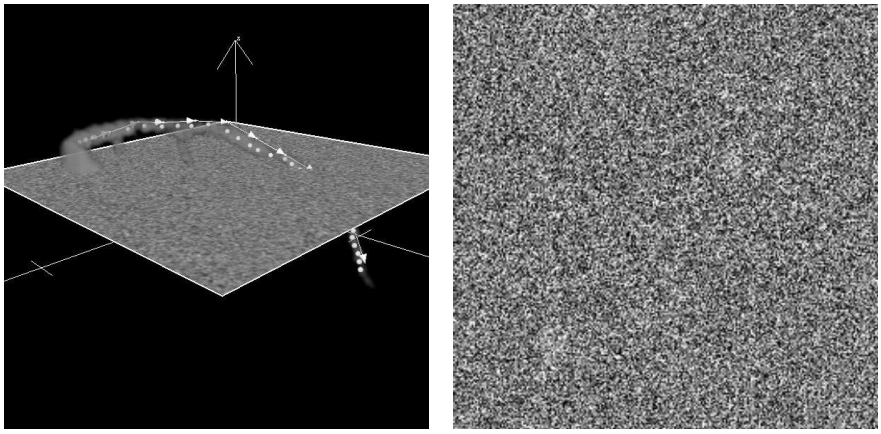

(a) (b)

Fig. 5. (a) An automatically found track (shown with arrows) in a simulated CTA dataset displayed together with the simulated dataset without noise, manual reference standard (white dots), and a slice from the dataset with noise. (b) shows the slice with noise in 2D.

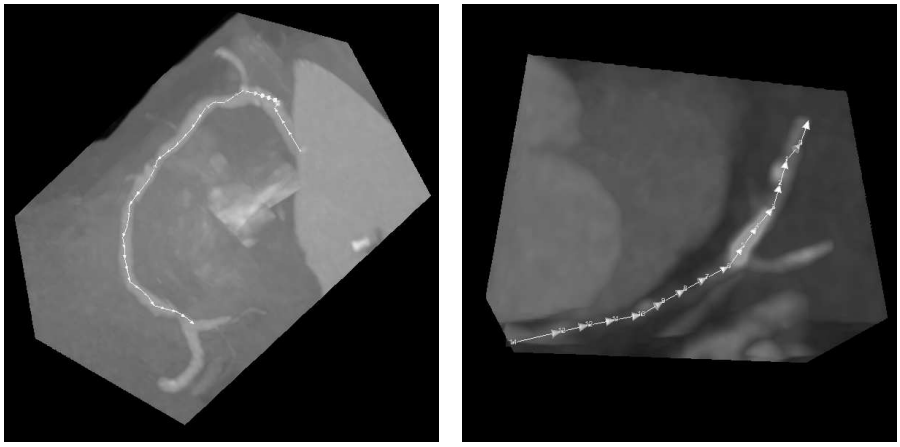

(a) (b)

Fig. 6. Examples of clinical applications of the probabilistic tracking algorithm. (a) shows a tracked right coronary artery in a CTA dataset. In (b) it is shown that an artery with a chronic total occlusion (CTO) in a CTA dataset is successfully tracked.

As a reference for values of MD we would like to refer to [5] and [12] for respectively tube enhancement and tracking. In [12] it is reported that straight tubes were successfully enhanced at MD > 5.3. The values presented in [5] are more difficult to compare, because varying tube radii were used, but indicative values can be obtained from this article.

The algorithm is also applied to 3D synthetic data (with a CNR of 0.25) and simulated high noise CTA data. Both tracks were found automatically with a RMSD of approximately 2 voxels to the reference standard. Furthermore, tracking results in real CTA data are presented, to demonstrate the clinical applicability of the proposed algorithm. The accuracy of the method is sufficient for using it as a first processing step in automated vessel quantification techniques.

Because probabilistic tube tracking algorithms are computationally complex, several computational improvements are suggested in this paper.

The development of automatic stopping criteria, bifurcation detection, and a comparison with existing deterministic and probabilistic algorithms are subject to future work.

The results are already promising for a wide variety of applications, but it should be noted that when using the presented algorithm for a specific application more a priori knowledge can be incorporated, such as expected intensity distributions and more specific observation models, and thereby probably improving the results.

7 Conclusion

A probabilistic tube tracking algorithm is presented in this article. The algorithm was evaluated on 2D synthetic data and tubes with $\mathrm{CNR}\sqrt{\mathrm{radius}} = 1.0$ were all

successfully tracked with accuracies that were in the same order of magnitude as the tracking results of the human observers. Furthermore, the approach was applied, with good performance, to 3D synthetic and clinical data.

Acknowledgment

This work was sponsored by the Dutch Foundation for Scientific Research, NWO, STW.

References

1. C. Caussin, C. Larchez, S. Ghostine, D. Pesenti-Rossi, B. Daoud, M. Habis, A. Sigal-Cinqualbre, E. Perrier, C.-Y. Angel, B. Lancelin, and J.-F. Paul, "Comparison of coronary minimal lumen area quantification by sixty-four-slice computed tomography versus intravascular ultrasound for intermediate stenosis.," *American Journal of Cardiology*, vol. 98, no. 7, pp. 871–876, 2006.
2. C. Kirbas and F. Quek, "A review of vessel extraction techniques and algorithms," *ACM Computing Surveys*, vol. 36, no. 2, pp. 81–121, 2004.
3. J. S. Suri, K. Liu, L. Reden, and S. Laxminarayan, "A review on MR vascular image processing algorithms: acquisition and prefiltering: part I," *IEEE Trans Inf Technol Biomed*, vol. 6, no. 4, pp. 324–337, 2002.
4. C. Florin, N. Paragios, and J. Williams, "Globally optimal active contours, sequential monte carlo and on-line learning for vessel segmentation.," in *ECCV (3)*, pp. 476–489, 2006.
5. S. Aylward and E. Bullit, "Initialization, noise, singularities, and scale in height ridge traversal for tubular object centerline extraction," *IEEE Transactions on Medical Imaging*, vol. 21, no. 2, pp. 61–75, 2002.
6. L. M. Lorigo, O. D. Faugeras, W. E. L. Grimson, R. Keriven, R. Kikinis, A. Nabavi, and C.-F. Westin, "Curves: Curve evolution for vessel segmentation," *Medical Image Analysis*, vol. 5, pp. 195–206, 2001.
7. D. Myatt, S. Nasuto, and S. Maybank, "Towards the automatic reconstruction of dendritic trees using particle filters," in *Linear Statistical Signal Processing Workshop (on CD-ROM)*, 2006.
8. A. Doucet, S. Godsill, and C. Andrieu, "On Sequential Monte Carlo Sampling Methods for Bayesian Filtering," *Statistics and Computing*, vol. 10, p. 197208, 2000.
9. E. W. Weisstein, "Rotation Matrix. From MathWorld–A Wolfram Web Resource.."
10. E. Saff and A. Kuijlaars, "Distributing many points on a sphere," *The Mathematical Intelligencer*, vol. 19, no. 1, pp. 5–11, 1997.
11. A. Rose, *Vision: Human and Electronic*. Plenum Press, New York, 1973.
12. R. Manniesing and W. Niessen, "Multiscale vessel enhancing diffusion in CT angiography noise filtering," in *Information Processing in Medical Imaging* (G. Christensen and M. Sonka, eds.), vol. 3565 of *Lecture Notes in Computer Science*, pp. 138–149, 2005.